Geophysical Research Letters

RESEARCH LETTER
10.1029/2018GL081697

Identification of Channeling in Pore-Scale Flows

Martina Siena[1], Oleg Iliev[2], Torben Prill[2], Monica Riva[1,3], and Alberto Guadagnini[1,3]

[1]Department of Civil and Environmental Engineering, Politecnico di Milano, Milan, Italy, [2]Fraunhofer Institute for Industrial Mathematics, Kaiserslautern, Germany, [3]Department of Hydrology and Atmospheric Sciences, University of Arizona, Tucson, AZ, USA

Key Points:
- Fast channels in 3-D pore-scale flow fields are identified as connected regions of the pore space where velocity outliers are found
- The topology of the network of pore bodies and throats forming the pore space drives spatial distributions of fast channels
- Fast channel size decreases as the Reynolds number increases and is related to the strength of preferential flow and anomalous transport

Supporting Information:
- Supporting Information S1

Correspondence to:
M. Siena,
martina.siena@polimi.it

Citation:
Siena, M., Iliev, O., Prill, T., Riva, M., & Guadagnini, A. (2019). Identification of channeling in pore-scale flows. *Geophysical Research Letters*, *46*, 3270–3278. https://doi.org/10.1029/2018GL081697

Received 14 DEC 2018
Accepted 9 MAR 2019
Accepted article online 13 MAR 2019
Published online 29 MAR 2019

Abstract We quantify flow channeling at the microscale in three-dimensional porous media. The study is motivated by the recognition that heterogeneity and connectivity of porous media are key drivers of channeling. While efforts in the characterization of this phenomenon mostly address processes at the continuum scale, it is recognized that pore-scale preferential flow may affect the behavior at larger scales. We consider synthetically generated pore structures and rely on geometrical/topological features of subregions of the pore space where clusters of velocity outliers are found. We relate quantitatively the size of such fast channels, formed by pore bodies and pore throats, to key indicators of preferential flow and anomalous transport. Pore-space spatial correlation provides information beyond just pore size distribution and drives the occurrence of these velocity structures. The latter occupy a larger fraction of the pore-space volume in pore throats than in pore bodies and shrink with increasing flow Reynolds number.

Plain Language Summary The movement of fluids and dissolved chemicals through porous media is massively affected by the heterogeneous nature of these systems. The presence of "fast channels," that is, preferential flow paths characterized by large velocities persisting over long distances, gives rise to very short solute travel times, with key implications in, for example, environmental risk assessment. While efforts in the characterization of this phenomenon mostly address processes at the continuum (laboratory or field) scale, it is recognized that pore-scale channeling of flow may affect the system behavior at larger scales. Here we provide criteria for the identification of fast channels at the pore scale, addressing feedback between channeling and geometrical/topological features of the investigated porous structures. Our results clearly evidence the major role of well-defined regions in the pore space, termed pore throats, in driving flow channeling. We also find that the strength of channeling is controlled by the characteristic Reynolds number of the flow field.

1. Introduction

Predictions of flow and transport processes in porous media are critically affected by the heterogeneous nature of pore spaces, intrinsically characterized by irregular geometrical features and properties that can vary widely across multiple spatial scales (Neuman, 2008; Neuman & Di Federico, 2003; Zami-Pierre et al., 2016). Notably, flow and transport phenomena are affected not only by the degree of heterogeneity of the medium but also by the spatial arrangement of its hydraulic properties, a prominent role being played by connectivity (Knudby & Carrera, 2005). While being seen as quite intuitive, the concept of connectivity is still lacking a formal and unambiguous definition. It can be regarded as a measure of the presence of preferential flow paths (or *fast channels*) across which flow tends to focus and be associated with high velocity values. Understanding the mechanisms driving flow to concentrate in high-velocity channels is key for proper prediction of first arrival times of dissolved chemicals at critical targets (Nissan & Berkowitz, 2018; Tartakovsky & Neuman, 2008; Zinn & Harvey, 2003) and the characterization of multiphase flow processes (Dai & Santamarina, 2013; Jiménez-Martínez et al., 2015), with direct implications in several settings, including, for example, environmental risk assessment or enhanced oil recovery. Channeling may occur under diverse conditions and on a wide range of spatial scales and is always characterized by two major features: (i) high velocity values persisting over long distances and (ii) flow focused within a few regions (principal paths) of the pore space (Hyman et al., 2012; Le Goc et al., 2010). Metrics suggested to quantify connectivity (Renard & Allard, 2013) are typically related to scenarios at the continuum (Darcy or field) scale and rely on the identification of connected paths of hydraulic properties (Dell'Arciprete et al., 2014; Le Goc et al., 2010) or of high-velocity patterns along flow trajectories (Fiori & Jankovic, 2012). While some indication about the level of channeling at the Darcy scale can be gained by

the correlation length of permeabilities, this is not the case at the pore scale. Characterization of channeling for two-dimensional geometries is presented in Alim et al. (2017) relying on the pore network method and in Nissan and Berkowitz (2018) solving Navier-Stokes equations for given pore geometries. Time evolution of the statistics of experimental observations of Lagrangian velocities in three-dimensional porous samples is analyzed in Carrel et al. (2018) to evaluate the effect of progressive biofilm growth on flow channeling.

In this Letter we propose a procedure to characterize quantitatively channeling phenomena at the pore level for three-dimensional voxelized geometries. This is achieved by (i) mapping the (continuous) velocity field into a categorical variable and (ii) studying geometrical and topological properties of the subregions of pore space associated with a given velocity class. The effectiveness of the approach proposed here is supported by the observation that our criteria lead to the quantification of a degree of channeling that is consistent with the magnitude of effects that channeling can have on flow and transport patterns documented at the continuum scale, resulting in preferential flow and anomalous transport (Bijeljic et al., 2011; De Anna et al., 2013; Kang et al., 2014, and reference therein).

2. Materials and Methods

2.1. Synthetic Pore Structure Generation

Let $\xi(-)$ be a (dimensionless) measure of channeling. The latter can be related to main governing quantities through the following functional form

$$\xi = f(\rho, \mu, V, L, \phi, \mathrm{pdf}_R), \tag{1}$$

where ρ (M/L^3) and μ (M·L^{-1}·T^{-1}) are fluid density and viscosity, respectively, V (L/T) is a characteristic velocity, L (L) represents the length size of (porous) domain, ϕ (−) is the sample porosity, and pdf_R is the probability density function of the pore size, R (L). We study ξ on synthetically generated, isotropic three-dimensional pore structures obtained on regular cubic grids from the convolution of a uniform distribution on [0,1] with a symmetric Gaussian kernel of width σ (Hyman & Winter, 2014). A binary image is obtained by allocating each cell of the grid either to the pore space or to the solid matrix, according to a level threshold $\gamma \in (0,1)$ applied to the generated random field. Let Ω_{pore} be the subset of grid cells that are associated with the pore space. Two cells in Ω_{pore}, identified by the coordinates of their centers ($\mathbf{x}_A$ and $\mathbf{x}_B$), are said to be connected if there exists a sequence of neighboring cells (i.e., of cells sharing a face) completely included in Ω_{pore} and linking $\mathbf{x}_A$ to $\mathbf{x}_B$. A group of connected cells is termed a *cluster*. For all blocks considered, the generation algorithm renders pore spaces exhibiting one dominant cluster. The final pore structures are obtained by removing all cells in Ω_{pore} that are not connected to the main cluster. It can be shown (Siena et al., 2014) that the two generation parameters, γ and σ, control porosity, ϕ, and mean pore size, $\langle R \rangle$, of the sample, respectively. The spatial correlation of the void space depends on both γ and σ. A key feature of the selected generator is that it allows reproducing sample pdf_R displaying exponential positive tails, the latter being consistently observed in samples of real porous systems (Holzner et al., 2015; Lindquist et al., 2000). Assuming that pdf_R can be approximated by an exponential distribution, equation (1) can be written in dimensionless form as

$$\xi = \bar{f}\left(\mathrm{Re}, \phi, \frac{\langle R \rangle}{L}\right), \tag{2}$$

$\mathrm{Re} = \rho V \langle R \rangle / \mu$ being the flow Reynolds number. In this Letter, we aim at assessing the impact of Re and $\langle R \rangle / L$, on the channeling metric ξ.

We generate three sets of cubic blocks, hereafter termed as sets 1, 2, and 3, each comprising a collection of 10 realizations. We set $L = 1.28$ cm, a voxel number $N = 128^3$ (i.e., voxel size $dl = 100$ μm), $\gamma = 0.45$ (which provided $\phi \approx \mathrm{const} = 0.4$), and we vary σ as 0.01, 0.03, or 0.05, for sets 1, 2, and 3, respectively. Figures 1a–1c depict cross-sectional contours of the inner structure of a representative block, termed as B_1, B_2, and B_3, from each of these sets.

2.2. Synthetic Pore Structure Topology

Geometrical and topological properties of the synthetic pore structures are inferred through a maximal ball (MB) algorithm. Among all spheres that are subsets of the pore space volume, MBs are those that are not fully contained in any other sphere. The pore-space skeleton can hence be identified as the set of points in

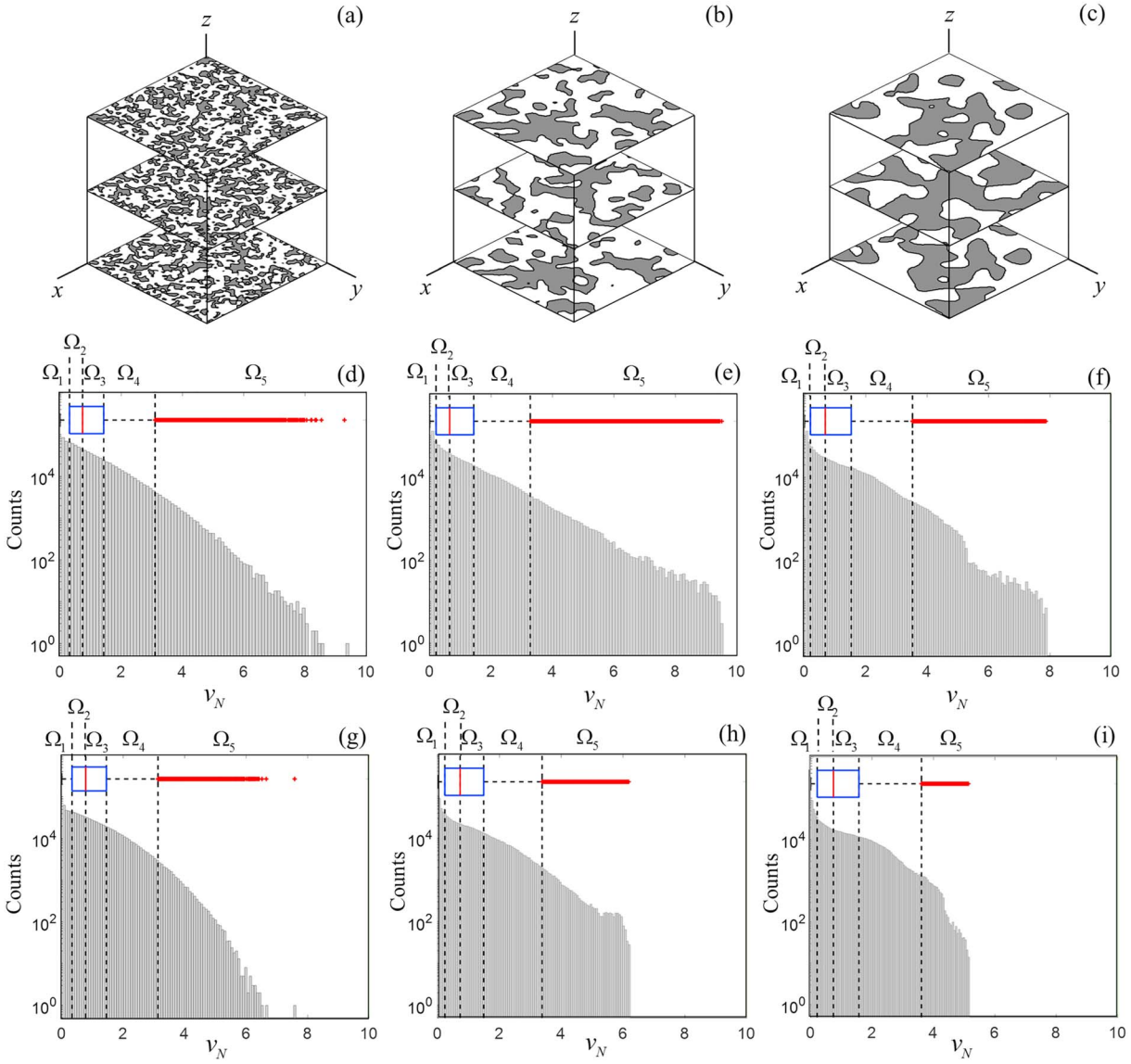

Figure 1. Cross-sectional contours of the pore space (gray areas) in B_1 (a), B_2 (b), and B_3 (c). Histograms of normalized velocity values, v_N, obtained in B_1, B_2, and B_3 for Re = 0.1 (d–f) and for Re = 10 (g–i). Box plots of v_N are also depicted to represent the thresholds used to define velocity classes (dashed lines).

the pore space that are centers of a MB (Silin & Patzek, 2006). The size R of a pore is then evaluated at each point of the pore-space skeleton as the radius of the largest sphere inscribed in the void space, measured by means of an inflating-deflating algorithm (Dong & Blunt, 2009). The (dimensionless) mean pore sizes, $\langle R \rangle / L$, of the three blocks depicted in Figures 1a–1c are 0.012, 0.036, and 0.050, respectively, for B_1, B_2, and B_3 (with averages of 0.011, 0.032, and 0.047 across block sets 1, 2, and 3). The MB algorithm also allows classifying each sphere according to a given type of topological element, that is, pore body (PB) or pore throat (PT; Dong & Blunt, 2009). Following this approach, each voxel in the void space is associated with a given pore size, R, and with the corresponding topological class.

2.3. Flow Simulations

We perform direct numerical simulations of steady-state, single-phase, fully saturated flow throughout the pore space of the generated blocks. We rely on the widely tested software GeoDict (from Math2Market GmbH, www.geodict.com) by setting (i) the mean velocity, V, at the inlet, $z = 0$, (ii) a constant pressure at the outlet, $z = L$, and (iii) impermeable lateral boundaries. GeoDict implements a finite volume scheme to

solve the Navier-Stokes equations, combining a SIMPLE algorithm with a Fast Fourier Transform approach to speed up the solution of the Poisson equation for pressure. Values of V at the inlet are set to obtain two diverse values of the Reynolds number for each block, that is, Re = 0.1, 10. Within this range of Re, Nissan and Berkowitz (2018) documented a transition from linear (Darcy) flow to nonlinear behavior in two-dimensional porous media.

3. Results and Discussion

3.1. Velocity Clusters

For ease of illustration, we focus here on results obtained in B_1, B_2, and B_3. Outcomes of similar quality are obtained for all of the blocks generated.

Histograms and box plots of (normalized) computed velocities, $v_N = |\mathbf{v}|/V$, $|\mathbf{v}|$ being the norm of the local velocity vector $\mathbf{v}$, obtained in B_1, B_2, and B_3 are depicted in Figures 1d–1f, respectively, for Re = 0.1 and in Figures 1g–1i for Re = 10. All plots are indicative of a common behavior of the computed velocity distributions, which are markedly right skewed, that is, skewed toward large values, for Re = 0.1. An increase of Re causes the extent of the support of the sample pdf of v_N to decrease, resulting in a more homogeneous flow field, a feature also observed by Nissan and Berkowitz (2018). These results are complemented by Figures S1 and S2 in the supporting information, depicting histograms of v_N values sampled in PBs and PTs.

We quantify channeling by introducing a categorical variable, $i = 1, ..., 5$. The latter is assigned to each voxel of the pore-space volume, Ω_{pore}, according to the following: $i = 1$ if $0 \le v_N < Q_1$; $i = 2$ if $Q_1 \le v_N < Q_2$; $i = 3$ if $Q_2 \le v_N < Q_3$; $i = 4$ if $Q_3 \le v_N < (Q_3+1.5IQR)$; and $i = 5$ if $v_N \ge (Q_3+1.5IQR)$, where $IQR = Q_3 - Q_1$ is the interquartile range, Q_1, Q_2, and Q_3 denoting the quartiles of the ranked set of v_N values. Note that, according to Tukey (1977), all values of a distribution which are larger than $Q_3 + 1.5\ IQR$ are regarded as mild outliers. The subregion of the pore space occupied by the categorical variable i is denoted as Ω_i. The study of clusters within Ω_i is aimed at identifying objects displaying the main features of channeling (i.e., large velocities which persist over long distances and are concentrated along only a few pathways) that are then used for a quantitative evaluation of these phenomena. We note that Ω_i becomes less fragmented (i.e., the total number of distinct clusters forming Ω_i decreases) as i increases, for all media and for both values of Re considered (see Tables S1 and S2). The mean cluster size shows a maximum for $i = 4$, a class which essentially contains one dominant cluster.

The connectivity function, $\tau_i^j(h)$, of category $i = 1, ..., 5$, along direction $j = \{x, y, z\}$, represents the probability that two cells in the same category and separated by a given distance are connected. According to Renard and Allard (2013), $\tau_i^j(h)$ can be computed as

$$\tau_i^j(h) = \frac{N\left(\mathbf{x}_A \leftrightarrow \mathbf{x}_B | \mathbf{x}_A \in \Omega_i, \mathbf{x}_B \in \Omega_i, \mathbf{x}_A - \mathbf{x}_B = h\mathbf{e}_j\right)}{N\left(\mathbf{x}_A \in \Omega_i, \mathbf{x}_B \in \Omega_i, \mathbf{x}_A - \mathbf{x}_B = h\mathbf{e}_j\right)}, \tag{3}$$

where the denominator $N(\mathbf{x}_A \in \Omega_i, \mathbf{x}_B \in \Omega_i, \mathbf{x}_A - \mathbf{x}_B = h\mathbf{e}_j)$ indicates the number of pairs of cells (identified by their centroids $(\mathbf{x}_A, \mathbf{x}_B)$) belonging to category i that are separated by a distance h along direction j (as represented by the unit vector $\mathbf{e}_j$). The numerator in equation (3) $N(\mathbf{x}_A \leftrightarrow \mathbf{x}_B | \mathbf{x}_A \in \Omega_i, \mathbf{x}_B \in \Omega_i, \mathbf{x}_A - \mathbf{x}_B = h\mathbf{e}_j)$ is the number of these pairs that also belong to the same cluster. Figure 2 collects graphical depictions of $\tau_i^j(h)$ in blocks B_1 (Figures 2a–2c), B_2 (Figures 2d–2f), and B_3 (Figures 2g–2i) for Re = 0.1. The largest separation distance h over which $\tau_i^j > 0$ provides a measure of the maximum extent of a single cluster of category i along direction j, $\ell_M^{i,j}$. We note that $\ell_M^{i,j}$ is roughly isotropic (i.e., it does not change with j) for classes $i = 1, ..., 4$ in all blocks considered. Class $i = 4$ in B_1 and classes $i = 2, 3, 4$ in both B_2 and B_3 have clusters spanning almost the whole extent of the block $\left(\ell_M^{i,j} \approx L\right)$. Close inspection of these classes reveals that these are essentially formed by a dominant cluster (with total size larger than 75% of the corresponding Ω_i) percolating in all directions, both parallel and normal to the mean flow direction, z. Such clusters are spread over the whole domain and are not concentrated within a few areas. Hence, they cannot be regarded as representative to quantify channeling. Otherwise, class $i = 5$ of v_N outliers exhibits a clear anisotropic behavior: The largest distance encompassed by a cluster in Ω_5 along the mean flow direction, $\ell_M^{5,z}$, is larger than its counterparts evaluated along the transverse directions x and y, $\ell_M^{5,x}$ and $\ell_M^{5,y}$ being less than 25% of the total block size. These features documented for τ_5^j support the choice of clusters associated with v_N outliers as a grounding element for the

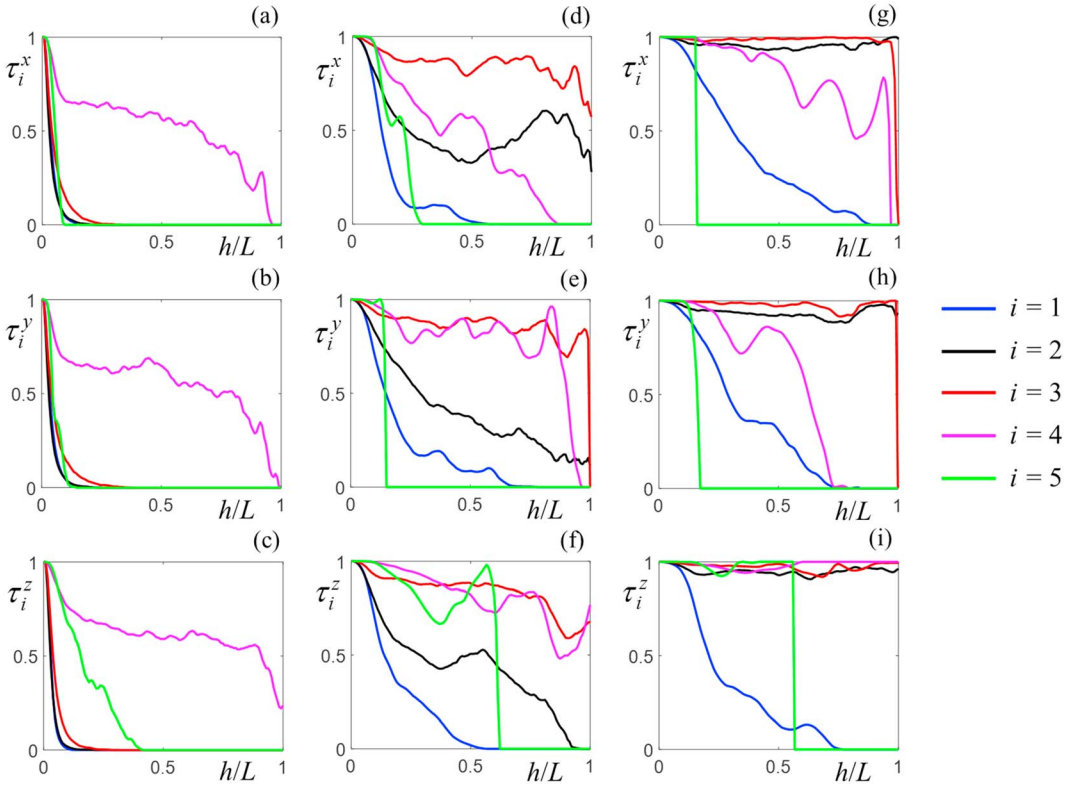

Figure 2. Connectivity function τ_i^j obtained for each velocity class ($i = 1, ..., 5$) along directions $j = x, y, z$, in B_1 (a–c), B_2 (d–f), and B_3 (g–i) for Re = 0.1.

characterization of channeling. Comparing the results obtained for the three porous systems studied, it can be noted that τ_5^j shows a near-stepwise behavior in B_2 (Figures 2d–2f) and B_3 (Figures 2g–2i), sharply dropping to 0 from values ≈1. Otherwise, values of τ_5^j in B_1 decreases smoothly with h, assuming values in the whole range [0, 1]. These results are indicative of a more fragmented Ω_5 domain in B_1, with generally more limited maximum lengths, $\ell_M^{5,j}$, as compared to B_2 and B_3. The most relevant effect of increasing Re is to reduce $\ell_M^{5,j}$ in all directions (see Figure S3).

3.2. Characterization of Fast Channels

We expect the relevance of channeling effects to be enhanced when high-velocity clusters are associated with enhanced persistence (i.e., in term of their elongation in the mean flow direction). We evaluate the cumulative distribution (*cdf*) of the longitudinal extent of clusters of velocity outliers, $\ell^{5,z}$, to identify the value of $\ell^{5,z}$ that corresponds to the 95th percentile of such a distribution. We regard as fast channels all clusters in Ω_5 having a longitudinal extent larger than this threshold, which corresponds to $L/2$ for B_2 and B_3 and to $L/3$ for B_1. Figures 3a and 3c depict the spatial pattern of the only cluster that fulfills this condition within block B_3, respectively, for Re = 0.1 and Re = 10. Note that each cell of the cluster is colored according to the associated type of topological element. The cluster encompasses both PBs and PTs, the large majority of the cluster volume being associated with PTs (green cells). A qualitative comparison between Figures 3a and 3c reveals that the cluster tends to shrink with increasing Re. This result is consistent with the findings of Nissan and Berkowitz (2018), where it is shown that an increase of Re is associated with an increased homogeneity of the flow field which, in turn, leads to a smaller amount of velocity outliers and, hence, a reduction of fast channel volume. An accurate characterization of the size of the above-identified cluster in Ω_5 can be obtained by application of the MB algorithm to its skeleton, to then evaluate the MB-based radius, R_5, associated with each point in the cluster. To investigate the relationship between Ω_5 clusters and the geometry/topology of the pore structures analyzed, we evaluate the ratio between R_5 and R within Ω_5. Since each cell is labeled according to the associated type of topological element, R_5/R can be computed separately for PBs and PTs. Figures 3b and 3d depict sample probability distribution functions of R_5/R,

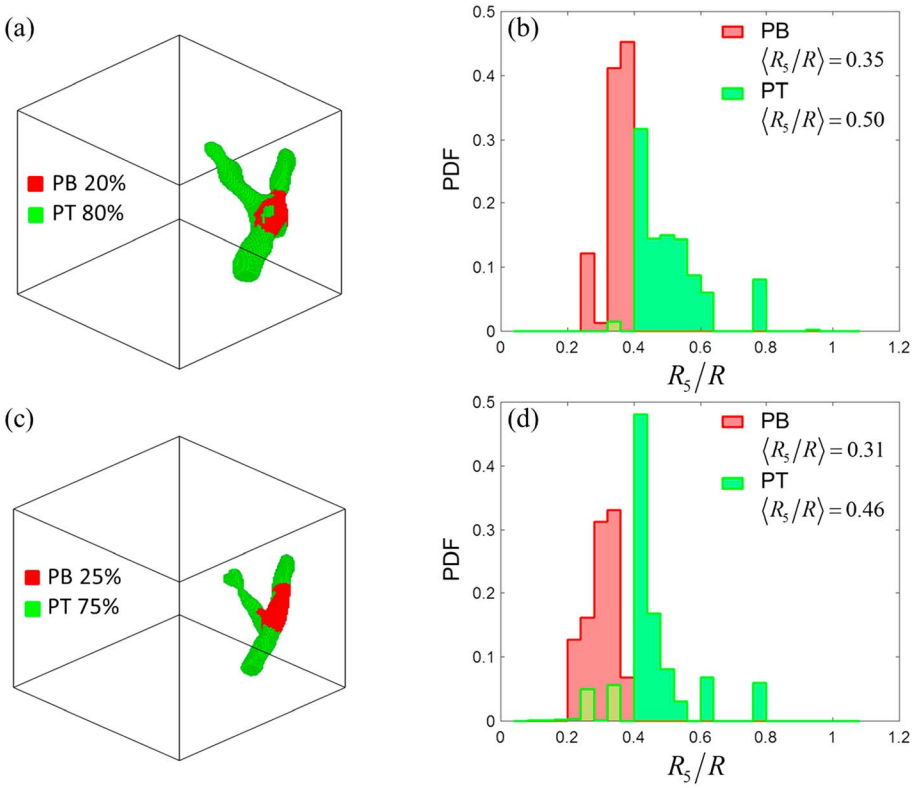

Figure 3. Block B_3: representation of the Ω_5 cluster having $\dot{e}^{5,z}$ above the 95th percentile for (a) Re = 0.1 and (c) Re = 10. Voxels belonging to PBs and PTs are, respectively, depicted in red and green. PDF of R_5/R evaluated in the selected Ω_5 cluster for PBs (red bars) and PTs (green bars) for (b) Re = 0.1 and (d) Re = 10. PB = pore body; PT = pore throat; PDF = probability distribution function.

respectively, for Re = 0.1 and Re = 10. In both plots, one can clearly note that the support of the probability distribution function in PTs (green bars) is wider and shifted toward larger values than the one of its PB counterparts (red bars). These findings suggest that the relative fraction of PT volume occupied by velocity outliers tends to be larger than its counterpart related to PBs. Similar results (see Figures S4 and S5) have been obtained for block B_2 and, to a limited extent, for block B_1.

3.3. Channeling Effects on Flow and Transport

To further support the ability of our criteria to identify channeling, we investigate links between the definition of fast channels introduced here and metrics typically employed to assess flow and transport features at the continuum scale. These include, for example, (i) the degree of preferential flow, as quantified by the participation number (Andrade et al., 1999; Nissan & Berkowitz, 2018), and (ii) deviations from Fickian transport behavior.

We follow Andrade et al. (1999) and Nissan and Berkowitz (2018) and consider the participation number as $\pi = \left(n\sum_{i=1}^{n} q_i^2\right)^{-1}$ (n is the total number of cells discretizing the pore space; $q_i = e_i/\sum_{j=1}^{n} e_j$; and $e_i = u_i^2 + v_i^2 + w_i^2$ is representative of the kinetic energy of a given cell; u_i, v_i, and w_i being the velocity components along x, y, and z axes, respectively). The kinetic energy is constant in all cells (i.e., π= 1) for a perfectly homogeneous flow. As preferential flow becomes more pronounced, π decreases. We evaluate this quantity in each flow field with Re = 0.1 and obtain $\overline{\pi} = 0.22$, 0.16, and 0.15 for sets 1, 2 and 3, respectively, the overbar representing the average over 10 realizations. These values indicate that sets 2 and 3 are characterized by a more pronounced preferential flow than set 1.

We also simulate transport of a passive chemical through an advective particle tracking approach (Russian et al., 2016) following injection of $N_P = 10^4$ particles uniformly distributed at the block inlet in each Eulerian

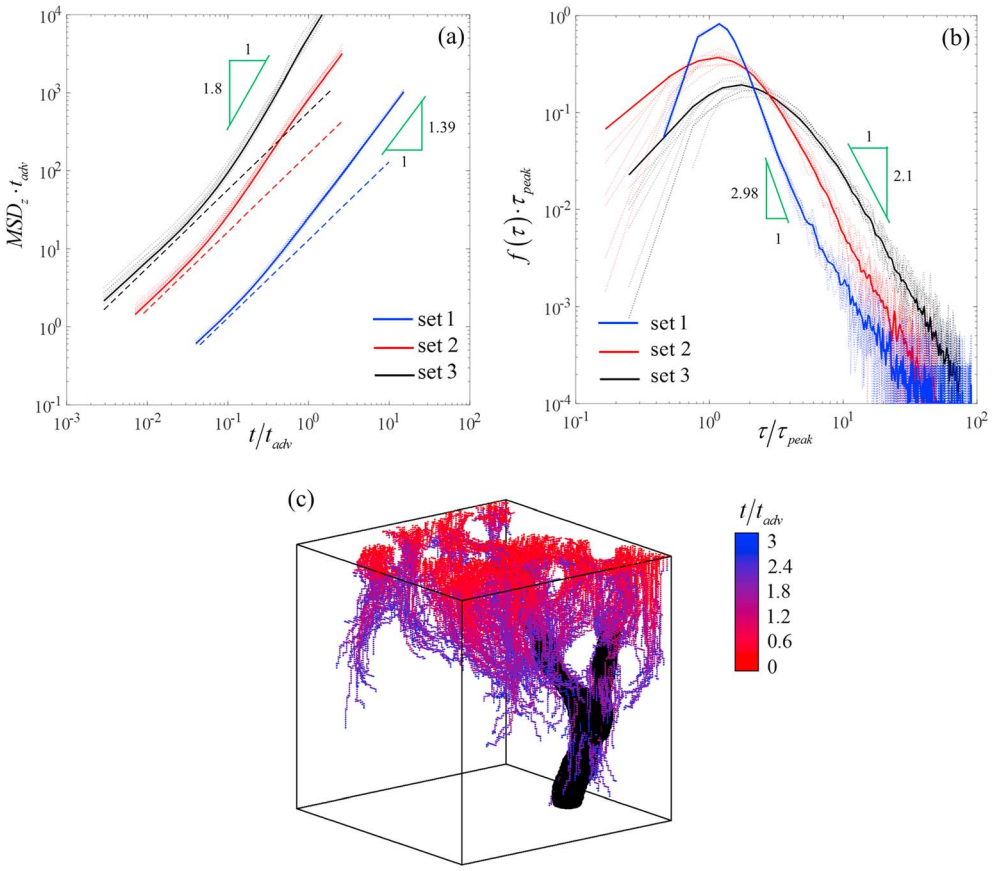

Figure 4. (a) Temporal evolution of the centered mean squared displacement along the z axis (MSD_z) averaged across the 10 realizations of sets 1, 2 and 3. Dashed lines correspond to Fickian behavior ($\propto t$). Results obtained for each pore-space realization are depicted (dotted curves). Time is rescaled by the advective travel time, t_{adv}. (b) First passage time distribution, $f(\tau)$, obtained by considering all particles in the 10 realizations for each block set. Results corresponding to each single realization are depicted (dotted curves). *FPTs* are rescaled by τ_{peak}, that is, the *FPT* at which the distribution peak is attained. (c) Fast channel (black volume) in B_3 for Re = 0.1 and associated particle trajectories (dotted curves) over a time range of $3t_{\mathrm{adv}}$. Colors represent (normalized) times at which a given position is reached.

steady-state flow field. We measure the average solute spreading in terms of centered mean squared displacement (*MSD*) along the main flow direction, $MSD_z(t) = \sum_{i=1}^{N_P} \left[z_i(t) - \mu_z(t)\right]^2 / N_P$, where $\mu_z(t) = \sum_{i=1}^{N_P} z_i(t) / N_P$, and distribution of first passage times ($FPT = \tau$), that is, the time required to a particle to reach the block outlet. Figure 4a depicts the temporal evolution of MSD_z obtained for Re = 0.1 by averaging over each set of 10 realizations (solid thick curves). All of these curves exhibit an asymptotic power-law scaling (with trend $\propto t^{\alpha}$) that deviates from the Fickian trend ($\propto t$, dashed thick lines). Estimates of the scaling exponent are $\alpha = 1.39$, 1.49, and 1.80 for sets 1, 2, and 3, respectively, indicating a more super-diffusive behavior in the latter. Figure 4b depicts the density distribution of first passage times, $f(\tau)$, obtained by considering all of the particles for each set of 10 realizations. The right tail is characterized by a power-law decay (with slope $\propto t^{-1-\beta}$) for all distributions, with $\beta = 1.98$, 1.58, and 1.10, for sets 1, 2, and 3, respectively. Note that the distribution of particle arrival times tends to broaden with decreasing β. These results further support the observation of a higher degree of anomalous transport behavior for set 3. Figure 4 also shows that the scaling behavior exhibited by MSD_z and $f(\tau)$ in each single realization (dotted thin curves) is very close to the one observed from the average over the whole set.

A clear connection between our proposed definition of fast channels (i.e., clusters in Ω_5 associated with values of $\mathscr{E}^{5,z}$ above the 95th percentile of the corresponding distribution) and the occurrence of anomalous transport is offered by Figure 4c. The latter depicts the fast channel identified in block B_3 for Re = 0.1, together with the trajectories of all injected particles over a time range of $3t_{\mathrm{adv}}$, where $t_{\mathrm{adv}} = \langle R \rangle / V$. The

lowest *FPT* evaluated for the system is equal to $2t_{adv}$ (not shown). The fast channel depicted in Figure 4c and identified according to our criteria is the portion of the pore space where particles with $FPTs \leq 3t_{adv}$ tend to focus. As such, it is the main driver of the heterogeneous longitudinal spreading of solute particles that could be inferred from the MSD_z and $f(\tau)$ curves.

We quantify flow channeling by means of volumetric size ($\xi_1 = \overline{W_{FC}}$) and longitudinal extent ($\xi_2 = \overline{\ell^{FC,z}}$) of fast channels, averaged over each set of 10 realizations. A quantitative relationship between the degree of preferential flow, anomalous transport, and our definition of fast channels can be inferred by comparing the participation number, $\overline{\pi}$, and the scaling exponents α and β with $\overline{W_{FC}}$ and $\overline{\ell^{FC,z}}$. For Re = 0.1, we obtain $\overline{W_{FC}}$ = 915, 10,330, and 27,122 voxels and $\overline{\ell^{FC,z}}$ = 56, 91, and 100 *dl*, for sets 1, 2, and 3, respectively. This result indicates that set 1, which is characterized by a more homogeneous flow pattern and by a less anomalous transport behavior, has a considerably smaller extent of fast channels with respect to sets 2 and 3.

All of these findings indicate that our definition of fast channels is directly related to continuum-scale features of flow and transport processes. We find analogous results considering the three sets of porous blocks for Re = 10. Further to this, as observed in section 3.2, fast channels tend to shrink along all directions as the flow Reynolds number increases in each set of pore structures (with $\overline{W_{FC}}$ = 406, 6,309, and 15,384 voxels and $\overline{\ell^{FC,z}}$ = 42, 82, and 83 *dl*). This behavior is consistent with the occurrence of increasingly homogeneous flow fields (as indicated by $\overline{\pi}$ = 0.27, 0.22, and 0.19) and decreased anomalous transport behavior (α = 1.37, 1.40, and 1.78; β = 2.8, 1.79, and 1.42), as compared against the scenarios for Re = 0.1.

4. Conclusions

In this Letter we propose formal criteria for the quantitative assessment of channeling phenomena at the pore level in three-dimensional voxelized synthetic pore structures. Key results of our study can be summarized as follows: (i) clusters of velocity outliers can be identified with fast channels, that is, preferential pathways/channels of flow, and this analogy enables us to delineate fast channels with a well-defined geometry; (ii) as the pore-space spatial correlation increases, the size of fast channels increases; (iii) fast channels tend to shrink along all directions as the flow Reynolds number increases; (iv) fast channels tend to occupy a larger fraction of the pore-space volume in PTs than they do in PBs; and (v) fast channels size can be related quantitatively to the degree of preferential flow and anomalous transport associated with a continuum-scale depiction of the system. These findings will serve as the basis for further investigation on a wider spectrum of pore-space models, aimed at identifying accurate statistically based geometrical and/or topological signatures of channeling phenomena.

Acknowledgments
This work was supported by the Fraunhofer Award for Young Researchers, established by the International Society for Porous Media, InterPore, in cooperation with the Fraunhofer institute for Industrial Mathematics, ITWM (Kaiserslautern). The authors would also like to thank the EU and MIUR for funding, in the frame of the collaborative international Consortium (WE-NEED) financed under the ERA-NET WaterWorks2014 Cofunded Call. This ERA-NET is an integral part of the 2015 Joint Activities developed by the Water Challenges for a Changing World Joint Programme Initiative (Water JPI). The data are available online (https://data.mendeley.com/datasets/mbzzyxc2cf/draft?a=68bfb0b3-5478-4eb6-bbe1-431ce6904575).

References

Alim, K., Parsa, S., Weitz, D. A., & Brenner, M. P. (2017). Local pore size correlations determine flow distributions in porous media. *Physical Review Letters*, *119*(14), 144,501. https://doi.org/10.1103/PhysRevLett.119.144501

Andrade, J. S., Costa, U. M. S., Almeida, M. P., Makse, H. A., & Stanley, H. E. (1999). Inertial effects on fluid flow through disordered porous media. *Physical Review Letters*, *86*(26), 5249. https://doi.org/10.1103/PhysRevLett.82.5249

Bijeljic, B., Mostaghimi, P., & Blunt, M. J. (2011). Signature of non-Fickian solute transport in complex heterogeneous porous media. *Physical Review Letters*, *107*(20), 204502. https://doi.org/10.1103/PhysRevLett.107.204502

Carrel, M., Morales, V. L., Dentz, M., Derlon, N., Morgenroth, E., & Holzner, M. (2018). Pore-scale hydrodynamics in a progressively bioclogged three-dimensional porous medium: 3-D particle tracking experiments and stochastic transport modeling. *Water Resources Research*, *54*, 2183–2198. https://doi.org/10.1002/2017WR021726

Dai, S., & Santamarina, J. C. (2013). Water retention curve for hydrate-bearing sediments. *Geophysical Research Letters*, *40*, 5637–5641. https://doi.org/10.1002/2013GL057884

De Anna, P., Le Borgne, T., Dentz, M., Tartakovsky, A. M., Bolster, D., & Davy, P. (2013). Flow intermittency, dispersion, and correlated continuous time random walks in porous media. *Physical Review Letters*, *110*(18), 184502. https://doi.org/10.1103/PhysRevLett.110.184502

Dell'Arciprete, D., Vassena, C., Baratelli, F., Giudici, M., Bersezio, R., & Felletti, F. (2014). Connectivity and single/dual domain transport models: Tests on a point-bar/channel aquifer analogue. *Hydrogeology Journal*, *22*(4), 761–778. https://doi.org/10.1007/s10040-014-1105-5

Dong, H., & Blunt, M. J. (2009). Pore-network extraction from micro-computerized-tomography images. *Physical Review E*, *80*(3), 036307. https://doi.org/10.1103/PhysRevE.80.036307

Fiori, A., & Jankovic, I. (2012). On preferential flow, channeling and connectivity in heterogeneous porous formations. *Mathematical Geosciences*, *44*(2), 133–145. https://doi.org/10.1007/s11004-011-9365-2

Holzner, M., Morales, V. L., Willmann, M., & Dentz, M. (2015). Intermittent Lagrangian velocities and accelerations in three-dimensional porous medium flow. *Physical Review E - Statistical, Nonlinear, and Soft Matter Physics*, *92*(1), 013015. https://doi.org/10.1103/PhysRevE.92.013015

Hyman, J. D., Smolarkiewicz, P. K., & Winter, C. L. (2012). Heterogeneities of flow in stochastically generated porous media. *Physical Review E*, *86*(5), 056701. https://doi.org/10.1103/PhysRevE.86.056701

Hyman, J. D., & Winter, C. L. (2014). Stochastic generation of explicit pore structures by thresholding Gaussian random fields. *Journal of Computational Physics*, *277*, 16–31. https://doi.org/10.1016/j.jcp.2014.07.046

Jiménez-Martínez, J., De Anna, P., Tabuteau, H., Turuban, R., Le Borgne, T., & Méheust, Y. (2015). Pore-scale mechanisms for the enhancement of mixing in unsaturated porous media and implications for chemical reactions. *Geophysical Research Letters*, *42*, 5316–5324. https://doi.org/10.1002/2015GL064513

Kang, P. K., De Anna, P., Nunes, J. P., Bijeljic, B., Blunt, M. J., & Juanes, R. (2014). Pore-scale intermittent velocity structure underpinning anomalous transport through 3-D porous media. *Geophysical Research Letters*, *41*, 6184–6190. https://doi.org/10.1002/2014gl061475

Knudby, C., & Carrera, J. (2005). On the relationship between indicators of geostatistical, flow and transport connectivity. *Advances in Water Resources*, *28*(4), 405–421. https://doi.org/10.1016/j.advwatres.2004.09.001

Le Goc, R., De Dreuzy, J., & Davy, P. (2010). Advances in water resources statistical characteristics of flow as indicators of channeling in heterogeneous porous and fractured media. *Advances in Water Resources*, *33*(3), 257–269. https://doi.org/10.1016/j.advwatres.2009.12.002

Lindquist, W. B., Venkatarangan, A., Dunsmuir, J., & Wong, T. (2000). Pore and throat size distributions measured from synchrotron X-ray tomographic images of Fontainebleau sandstones. *Journal of Geophysical Research*, *105*(B9), 21,509–21,527. https://doi.org/10.1029/2000JB900208

Neuman, S. P. (2008). Multiscale relationships between fracture length, aperture, density and permeability. *Geophysical Research Letters*, *35*, L22402. https://doi.org/10.1029/2008GL035622

Neuman, S. P., & Di Federico, V. (2003). Multifaceted nature of hydrogeologic scaling and its interpretation. *Reviews of Geophysics*, *41*(3), 1014. https://doi.org/10.1029/2003RG000130

Nissan, A., & Berkowitz, B. (2018). Inertial effects on flow and transport in heterogeneous porous media. *Physical Review Letters*, *120*(5), 54504. https://doi.org/10.1103/PhysRevLett.120.054504

Renard, P., & Allard, D. (2013). Connectivity metrics for subsurface flow and transport. *Advances in Water Resources*, *51*, 168–196. https://doi.org/10.1016/j.advwatres.2011.12.001

Russian, A., Dentz, M., & Gouze, P. (2016). Time domain random walks for hydrodynamic transport in heterogeneous media. *Water Resources Research*, *52*, 3309–3323. https://doi.org/10.1002/2015WR018511

Siena, M., Riva, M., Hyman, J. D., Winter, C. L., & Guadagnini, A. (2014). Relationship between pore size and velocity probability distributions in stochastically generated porous media. *Physical Review E*, *89*(1), 013018. https://doi.org/10.1103/PhysRevE.89.013018

Silin, D., & Patzek, T. (2006). Pore space morphology analysis using maximal inscribed spheres. *Physica A: Statistical Mechanics and its Applications*, *371*(2), 336–360. https://doi.org/10.1016/j.physa.2006.04.048

Tartakovsky, A. M., & Neuman, S. P. (2008). Effects of Peclet number on pore-scale mixing and channeling of a tracer and on directional advective porosity. *Geophysical Research Letters*, *35*, L21401. https://doi.org/10.1029/2008GL035895

Tukey, J. W. (1977). *Exploratory Data Analysis*. Reading, PA: Addison-Wesley.

Zami-Pierre, F., de Loubens, R., Quintard, M., & Davit, Y. (2016). Transition in the flow of power-law fluids through isotropic porous media. *Physical Review Letters*, *117*(7), 074502. https://doi.org/10.1103/PhysRevLett.117.074502

Zinn, B., & Harvey, C. F. (2003). When good statistical models of aquifer heterogeneity go bad: A comparison of flow, dispersion, and mass transfer in connected and multivariate Gaussian hydraulic conductivity fields. *Water Resources Research*, *39*(3), 1051. https://doi.org/10.1029/2001WR001146